

Frequency chirp-induced enhancement of electron–positron pair production in polarized laser fields

Obulkasim Olugh(吾布力卡斯木·吾鲁克)

Citation: Chin. Phys. B, 2026, 35 (**4**): 045202. DOI: 10.1088/1674-1056/ae0a3c
http://cpb.iphy.ac.cn; http://iopscience.iop.org/cpb

What follows is a list of articles you may be interested in

Effect of sharp vacuum-plasma boundary on the electron injection and acceleration in a few-cycle laser driven wakefield

Guo-Bo Zhang(张国博), Song Liu(刘松), De-Bin Zou(邹德滨), Ye Cui(崔野), Jian-Peng Liu(刘建鹏), Xiao-Hu Yang(杨晓虎), Yan-Yun Ma(马燕云), and Fu-Qiu Shao(邵福球)
Chin. Phys. B, 2023, 32 (**9**): 095202. DOI: 10.1088/1674-1056/acdc0c

Femtosecond laser-induced Cu plasma spectra at different laser polarizations and sample temperatures

Yitong Liu(刘奕彤), Qiuyun Wang(王秋云), Luyun Jiang(蒋陆昀), Anmin Chen(陈安民), Jianhui Han(韩建慧), and Mingxing Jin(金明星)
Chin. Phys. B, 2022, 31 (**10**): 105201. DOI: 10.1088/1674-1056/ac6864

Ultrabright γ-ray emission from the interaction of an intense laser pulse with a near-critical-density plasma

Aynisa Tursun(阿依妮萨·图尔荪), Mamat Ali Bake(买买提艾力·巴克), Baisong Xie(谢柏松), Yasheng Niyazi(亚生·尼亚孜), and Abuduresuli Abudurexiti(阿不都热苏力·阿不都热西提)
Chin. Phys. B, 2021, 30 (**11**): 115202. DOI: 10.1088/1674-1056/abfb59

Influence of polarization of laser beam on emission intensity of femtosecond laser-induced breakdown spectroscopy

Lan Yang(杨岚), Miao Liu(刘淼), Yi-Tong Liu(刘奕彤), Qing-Xue Li(李庆雪), Su-Yu Li(李苏宇), Yuan-Fei Jiang(姜远飞), An-Min Chen(陈安民), Ming-Xing Jin(金明星)
Chin. Phys. B, 2020, 29 (**6**): 065203. DOI: 10.1088/1674-1056/ab84dc

---

Frequency chirp-induced enhancement of electron–positron pair production in polarized laser fields

Obulkasim Olugh(吾布力卡斯木·吾鲁克)[†]

Department of Forensic Science and Technology, Xinjiang Police College, Urumqi 830013, *China*

(Received 4 August 2025; revised manuscript received 12 September 2025; accepted manuscript online 23 September 2025)

We investigate electron–positron pair production in frequency-chirped, polarized laser fields using the Dirac–Heisenberg–Wigner formalism. A key theoretical finding is the polarization-dependent critical chirp threshold $b_c(\delta)$, which marks the transition between tunneling-dominated and multiphoton pair production regimes: b_c doubles as polarization evolves from linear ($\delta = 0$, $b_c(0) = 0.02$ m^2) to circular ($\delta = 1$, $b_c(1) = 0.04$ m^2). Above this threshold, chirp induces spectral compression with the momentum distribution width scaling as $\Delta q \propto b^{-1/2}$, concentrating pairs into a smaller phase-space volume and enhancing production yields by up to three orders of magnitude, following the universal scaling law $n \propto (b\tau)^{3/2}$. Notably, non-monotonic polarization dependence is observed at intermediate chirp values, where linear polarization temporarily surpasses circular in yield before convergence at large b. These results establish chirp as a precise control parameter for optimizing EP pair production in nonperturbative quantum electrodynamics, advancing the theoretical framework for understanding quantum vacuum dynamics and providing a foundation for structured pulse engineering in strong-field quantum electrodynamics.

Keywords: electron–positron pair production, frequency chirp, laser polarization, Dirac–Heisenberg–Wigner formalism, strong-field QED, spectral compression, critical threshold

PACS: 52.38.–r, 12.20.–m, 13.40.–f

DOI: 10.1088/1674-1056/ae0a3c **CSTR:** 32038.14.CPB.ae0a3c

1. Introduction

Electron–positron (e^-e^+) pair production in strong electromagnetic fields represents one of the most profound predictions of quantum electrodynamics (QED), first proposed by F. Sauter in 1931[1] and independently developed by W. Heisenberg and H. Euler in 1936.[2] These foundational works established the theoretical framework for understanding vacuum polarization and nonperturbative particle creation in external fields. The modern formulation of the Schwinger formula[3] quantifies pair production in spatially homogeneous, static electric fields, with the critical field strength $E_{\rm cr} = m^2c^3/e\hbar \approx 1.3 \times 10^{18}$ V/m (corresponding to a laser intensity $I = 4.3 \times 10^{29}$ W/cm^2) marking the threshold for significant pair production. While this regime remains experimentally inaccessible with current technology, advances in high-intensity laser facilities such as x-ray free electron lasers (XFELs) — including the European XFEL and Linac Coherent Light Source — are pushing the boundaries of achievable field strengths.[4–6] These facilities, capable of reaching subcritical fields ($E \sim 0.1E_{\rm cr}$) with peak intensities up to 10^{20} W/cm^2,[7,8] offer a promising path toward observing the Sauter–Schwinger effect in the near future.

The e^-e^+ pair creation from the QED vacuum constitutes a paradigmatic example of nonperturbative and nonequilibrium quantum dynamics. Significant theoretical progress has been made in addressing these challenges through various approximation methods. These include the WKB approximation,[9–11] its refined extension via worldline instanton techniques,[12–16] and quantum kinetic approaches based on the quantum Vlasov equation.[7,17–21] Additionally, the Wigner function formalism[22–37] has proven effective for studying vacuum pair production in external fields. For detailed information on the various approaches, refer to the comprehensive review of pair production mechanisms.[38]

The production of e^-e^+ pairs has been extensively studied in increasingly complex and realistic field configurations. Using the quantum kinetic approach, Ref. [39] demonstrated that the momentum spectrum of produced particles exhibits strong sensitivity to the subcycle structure of linearly polarized electric fields. Subsequent work[40] further analyzed how particle production depends on the detailed temporal profile of external fields.

For more sophisticated field configurations, the Dirac–Heisenberg–Wigner (DHW) formalism has emerged as a powerful theoretical framework for studying vacuum pair production.[22–24] This approach offers significant advantages: it provides a fully relativistic phase-space description of quantum field dynamics,[22] maintains full covariance, and enables real-time numerical simulations. Recent applications of the DHW formalism have demonstrated its utility in analyzing rotating, time-dependent circularly polarized fields,[27] where characteristic momentum distributions distinguish between

[†]Corresponding author. E-mail: obulkasimolugh@163.com

© 2026 Chinese Physical Society and IOP Publishing Ltd. All rights, including for text and data mining, AI training, and similar technologies, are reserved.

QED cascades initiated by pair production and isotropic vacuum fluctuations. Numerical studies[26] have further revealed that increasing field polarization leads to pronounced circular distortions in the momentum distribution of created particles, along with spectral splitting in few-cycle field regimes.

Table 1. Comparison of field parameters between this work and previous studies. The extended pulse duration $\tau = 16/m$ (vs. $\tau = 10/m$ in Ref. [31]) enhances adiabaticity effects, while the reduced frequency $\omega = 0.5m$ (vs. $\omega = 0.6m$) better matches current optical laser capabilities.

Study	E_0	ω	τ
Ref. [31]	$0.1\sqrt{2}E_{\rm cr}$	$0.6m$	$10/m$
This work	$0.2\sqrt{2}E_{\rm cr}$	$0.5m$	$16/m$

The rapid advancement of high-intensity laser technology has opened new frontiers in strong-field QED, enabling unprecedented control over both the temporal and polarization properties of electromagnetic fields. While seminal works by Blinne and Gies[27] established the foundational understanding of pair production in rotating, time-dependent circularly polarized fields, and our previous study[31] provided the first comprehensive analysis of frequency-chirped fields, a systematic investigation of the combined effects of chirp and polarization remains an important frontier. This gap is particularly significant given that modern laser facilities such as the Extreme Light Infrastructure (ELI) and Station of Extreme Light (SEL) now enable precise, independent control of both frequency chirp and polarization state within the same pulse.[41]

The theoretical exploration of this combined parameter space is motivated by several compelling reasons. First, the chirp parameter b introduces a dynamic element to the field frequency $\omega_{\rm eff}(t) = \omega + bt$, which fundamentally alters the resonance conditions for pair production across different polarization states. Second, as demonstrated by the characteristic momentum distributions in Ref. [27], polarization state significantly influences the geometric structure of the produced pairs, suggesting that the interplay between chirp-induced spectral compression and polarization-dependent selection rules could reveal novel enhancement mechanisms. Third, the critical transition between tunneling-dominated and multiphoton regimes, first identified in Ref. [31], may exhibit previously unobserved polarization dependence when chirp is properly incorporated into the theoretical framework.

Motivated by these considerations and the experimental capabilities of next-generation laser facilities, we systematically investigate electron–positron pair production in chirped, polarized laser fields using the DHW formalism. Our work extends the foundational studies of Blinne and Gies[27] and our previous chirp analysis[31] by providing the first unified theoretical framework that simultaneously accounts for both frequency modulation and polarization effects, revealing the polarization-dependent critical chirp threshold $b_{\rm c}(\delta)$ and the universal scaling law $n \propto (b\tau)^{3/2}$ that characterize this previously unexplored parameter space.

The electric field configuration is

$$\boldsymbol{E}(t) = \frac{E_0}{\sqrt{1+\delta^2}}\, {\rm e}^{-t^2/2\tau^2} \begin{pmatrix} \cos(bt^2+\omega t+\varphi) \\ \delta \sin(bt^2+\omega t+\varphi) \\ 0 \end{pmatrix}, \quad (1)$$

where $E_0/\sqrt{1+\delta^2}$ is the field amplitude, τ the pulse duration, ω the central frequency at $t = 0$, b the chirp parameter, and δ the polarization parameter (ellipticity). The chirp parameter b quantifies the rate of change of the laser's instantaneous frequency with time. A non-zero b introduces a quadratic time dependence to the laser phase, $\phi(t) = \omega t + bt^2$, resulting in a linearly time-varying instantaneous frequency, $\omega_{\rm eff}(t) = {\rm d}\phi/{\rm d}t = \omega + 2bt$. This time-dependent frequency modulation dynamically tunes the pair production mechanism during the pulse, transitioning the system from tunneling-dominated to multiphoton-dominated regimes as b increases. In standard optics literature, this is referred to as a "linear frequency chirp" due to the linear dependence of $\omega_{\rm eff}(t)$ on time. For completeness, we retain the carrier phase φ in this expression because it is known to significantly influence the momentum spectra of the produced pairs.[18] However, for simplicity and without loss of generality, we set $\varphi = 0$ in the following analysis.

It is worth noting that the purely time-dependent electric fields given in Eq. (1) can be regarded as the dipole approximation of a standing wave formed by two counterpropagating laser beams with different polarizations. The primary focus of this study, however, is on the dependence of the pair production process on the chirp parameter b.

In this work, we focus on chirp parameters within the range $0 \le b \le \omega/\tau$. These values represent typical "nominal chirps" (small to moderate values) and an upper bound corresponding to the maximal chirp magnitude $b = \omega/\tau$. A non-vanishing b introduces a time-dependent effective frequency, $\omega_{\rm eff} = \omega + bt$, which modulates the pair production mechanism.

This study extends our previous work[31] by introducing three key innovations: (1) we identify and characterize a critical chirp threshold $b_{\rm c}$ that separates tunneling-dominated and multiphoton regimes, which depends explicitly on the polarization state δ; (2) we demonstrate chirp-induced spectral compression ($\Delta q \propto b^{-1/2}$) as a universal mechanism for enhancing pair production across different polarization states; (3) we establish a universal scaling law $n \propto (b\tau)^{3/2}$ that bridges field configurations and provides a design principle for optimizing pair production in experimental setups.

The parameter choice $E_0 = 0.2\sqrt{2}E_{\rm cr}$, $\omega = 0.5m$, and $\tau = 16/m$ represents a deliberate optimization for studying chirp effects, as shown in Table 1. Compared to our previous study,[31] the reduced frequency $\omega = 0.5m$ (vs. $\omega = 0.6m$) better matches current optical laser capabilities and enhances

multiphoton absorption processes. The extended pulse duration $\tau = 16/m$ (vs. $\tau = 10/m$) enhances adiabaticity effects in the chirped field regime, allowing clearer observation of chirp-induced spectral distortions and transitions between production mechanisms.

To characterize the production mechanism, we introduce the Keldysh adiabaticity parameter $\gamma(t) = \frac{m\omega_{\rm eff}(t)}{|eE(t)|}$, where $\omega_{\rm eff}(t) = \omega + bt$ and $E(t) = E_0\,{\rm e}^{-t^2/(2\tau^2)}$. This parameter distinguishes between Schwinger (tunneling) pair production ($\gamma(t) \ll 1$) and multiphoton pair production ($\gamma(t) \gg 1$).[42] For the given parameters, the initial Keldysh parameter evaluates to $\gamma_0 = 1.77\sqrt{1+\delta^2}$ for each polarization state, placing the system near the transition between multiphoton and tunneling regimes ($\gamma \sim 1$). When chirp is introduced ($b \neq 0$), the time-dependent modulation shifts the production mechanism from predominantly multiphoton ($\gamma(t) \gtrsim 1$) toward a hybrid regime with tunable Schwinger-like contributions as chirp increases.

The specific field configuration described by Eq. (1) with our chosen parameters ($E_0 = 0.2\sqrt{2}E_{\rm cr} \approx 3.68 \times 10^{17}$ V/m, $\omega = 0.5m$, $\tau = 16/m$) represents a theoretically accessible regime for next-generation laser facilities. For an electron mass $m = 0.511$ MeV, the frequency corresponds to wavelength $\lambda = 2\pi c/\omega \approx 4.85$ pm (x-ray regime), while the pulse duration $\tau \approx 2.06 \times 10^{-20}$ s (0.0206 as) is beyond current technological capabilities but serves to explore fundamental physics. The peak intensity is $I \approx 1.8 \times 10^{28}$ W/cm^2, which is within reach of upcoming facilities such as ELI and SEL.

Using the real-time DHW formalism,[22,23] we systematically investigate how chirp parameters influence the momentum spectra and number density of e^+e^- pairs in time-dependent electric fields with linear, elliptical, and circular polarizations. Our numerical calculations provide complete momentum distribution functions and quantify the dependence of pair production yields on chirp parameters across different polarization states.

This paper is organized as follows. In Section 2, we present a self-contained derivation of the DHW formalism with particular attention to the mathematical steps connecting the Dirac equation to the phase-space transport equations. In Section 3, we analyze the numerical results with emphasis on the physical mechanisms behind chirp-induced enhancements, including symmetry breaking effects and spectral compression phenomena. In Section 4, we summarize our main results and outline future research directions.

2. Dirac–Heisenberg–Wigner formalism

The DHW formalism provides a fully relativistic phase-space description of quantum field dynamics,[22,30] which is particularly well suited for studying nonperturbative phenomena such as electron–positron pair production in strong and time-dependent electromagnetic fields.[23] Unlike alternative approaches that either focus on static fields or employ perturbative treatments, the DHW method uniquely captures the real-time evolution of quantum fields under rapidly varying external conditions. This capability makes it especially valuable for investigating frequency-chirped fields where the time-dependent modulation of the effective frequency $\omega_{\rm eff}(t) = \omega + bt$ requires a nonperturbative, time-resolved description.

The primary advantage of the DHW formalism for our study lies in its ability to simultaneously handle three critical aspects: (1) the full relativistic structure of QED, (2) time-dependent field configurations with arbitrary polarization states, and (3) the nonperturbative nature of pair production near the Schwinger limit. As demonstrated below, this framework naturally reveals the geometric structures and scaling laws that emerge from the interplay between chirp and polarization.

2.1. Foundations: from dirac equation to phase-space representation

The starting point is the Dirac equation for the electron field operator $\hat{\psi}$ in an external electromagnetic field:

$$(\mathrm{i}\gamma^\mu \partial_\mu - e\gamma^\mu A_\mu - m)\hat{\psi} = 0, \tag{2}$$

where γ^μ are the Dirac matrices, A_μ is the electromagnetic four-potential, and m is the electron mass. To construct a phase-space representation, we consider the two-point correlation function

$$\hat{\mathcal{C}}_{\alpha\beta}(x_1,x_2) = \left\langle 0 \middle| \left\{ \hat{\bar{\psi}}_\beta(x_2), \hat{\psi}_\alpha(x_1) \right\} \middle| 0 \right\rangle. \tag{3}$$

The use of the anticommutator ensures the gauge invariance and correct fermionic statistical properties of the constructed Wigner function.

For spatially homogeneous fields, it is convenient to introduce center-of-mass and relative coordinates:

$$\boldsymbol{r} = \frac{\boldsymbol{x}_1 + \boldsymbol{x}_2}{2}, \quad \boldsymbol{s} = \boldsymbol{x}_1 - \boldsymbol{x}_2, \quad t = \frac{t_1 + t_2}{2}. \tag{4}$$

The key insight of the DHW formalism is that in the presence of an electromagnetic field, this correlation function must be made gauge-invariant by inserting a Wilson line factor

$$\begin{aligned}&\hat{\mathcal{C}}_{\alpha\beta}(\boldsymbol{r},\boldsymbol{s},t) \\ &= \mathcal{U}(A;\boldsymbol{r},\boldsymbol{s}) \left\langle 0 \middle| \left\{ \hat{\bar{\psi}}_\beta\left(\boldsymbol{r} - \frac{\boldsymbol{s}}{2}, t\right), \hat{\psi}_\alpha\left(\boldsymbol{r} + \frac{\boldsymbol{s}}{2}, t\right) \right\} \middle| 0 \right\rangle,\end{aligned} \tag{5}$$

where the Wilson line ensures gauge invariance

$$\mathcal{U}(A;\boldsymbol{r},\boldsymbol{s}) = \exp\left(-\mathrm{i}e \int_{-1/2}^{1/2} \mathrm{d}\lambda\, \boldsymbol{s}\cdot\boldsymbol{A}(\boldsymbol{r} + \lambda\boldsymbol{s}, t) \right). \tag{6}$$

The Wigner operator is then obtained via Fourier transformation with respect to $\boldsymbol{s}$:

$$\hat{\mathcal{W}}_{\alpha\beta}(\boldsymbol{r},\boldsymbol{p},t) = \frac{1}{2}\int \mathrm{d}^3 s\, {\rm e}^{-\mathrm{i}\boldsymbol{p}\cdot\boldsymbol{s}}\, \hat{\mathcal{C}}_{\alpha\beta}(\boldsymbol{r},\boldsymbol{s},t). \tag{7}$$

Taking the vacuum expectation value yields the quantum phase-space distribution function

$$\mathbb{W}(\boldsymbol{r},\boldsymbol{p},t) = \langle 0|\hat{\mathcal{W}}(\boldsymbol{r},\boldsymbol{p},t)|0\rangle. \tag{8}$$

2.2. Mathematical derivation of evolution equations

To derive the evolution equations, we substitute the Dirac equation (2) into the correlation function. For spatially homogeneous fields, $\mathbb{W}$ becomes independent of $\boldsymbol{r}$, and we can work in momentum space with the canonical momentum $\boldsymbol{q} = \boldsymbol{p} + e\boldsymbol{A}(t)$.

The crucial step involves applying the Dirac equation to both $\hat{\psi}(x_1)$ and $\hat{\bar{\psi}}(x_2)$, which leads to

$$\begin{aligned} \mathrm{i}\partial_t \mathbb{W}_{\alpha\beta}(\boldsymbol{q},t) \;=\; & \left[\frac{1}{2}\{\gamma^0(m-\boldsymbol{\gamma}\cdot\boldsymbol{q}),\mathbb{W}\}\right]_{\alpha\beta} \\ & + \frac{1}{2}\int_{-\infty}^{\infty}\frac{\mathrm{d}\eta}{\pi\eta}\,\mathrm{e}^{\,\mathrm{i}\eta\partial_q}\left[\gamma^0 e\boldsymbol{E}(t)\cdot\nabla_{\boldsymbol{q}}\mathbb{W}\right]_{\alpha\beta}, \end{aligned} \tag{9}$$

where the second term contains the pseudodifferential operator representing the electric field interaction. For homogeneous fields, this reduces to the transport-like equation

$$(\partial_t + e\boldsymbol{E}(t)\cdot\nabla_{\boldsymbol{q}})\,\mathbb{W}(\boldsymbol{q},t) = -\mathrm{i}\left[\gamma^0(m-\boldsymbol{\gamma}\cdot\boldsymbol{q}),\mathbb{W}(\boldsymbol{q},t)\right]. \tag{10}$$

2.3. Phase-space decomposition and component reduction

The 4×4 spinor-valued Wigner function can be decomposed into 16 independent components using the Clifford algebra basis:

$$\mathbb{W} = \frac{1}{4}\left(\mathbb{1}\mathbb{S} + \mathrm{i}\gamma_5\mathbb{P} + \gamma^\mu\mathbb{V}_\mu + \gamma^\mu\gamma_5\mathbb{A}_\mu + \sigma^{\mu\nu}\mathbb{T}_{\mu\nu}\right), \tag{11}$$

where $\mathbb{S}$: scalar component (related to mass density), $\mathbb{P}$: pseudoscalar (chirality), $\mathbb{V}_\mu$: vector (charge and current densities), $\mathbb{A}_\mu$: axial vector (spin polarization), $\mathbb{T}_{\mu\nu}$: antisymmetric tensor (anisotropic stress or polarization).[43]

For spatially homogeneous electric fields with $\boldsymbol{B} = 0$, rotational symmetry reduces the number of independent components to 10. Specifically, for fields polarized in the xy-plane (as in our case), the non-vanishing components are $\mathbb{S}$, $\mathbb{V}_x$, $\mathbb{V}_y$, $\mathbb{A}_z$, $\mathbb{T}_{xz}$, $\mathbb{T}_{yz}$, $\mathbb{T}_{xy}$, $\mathbb{T}_{0x}$, $\mathbb{T}_{0y}$, and $\mathbb{T}_{0z}$.

Substituting the decomposition into Eq. (10) and equating coefficients of the basis elements yields the reduced system of equations. After detailed algebraic manipulation, we obtain the transport equation

$$(\partial_t + e\boldsymbol{E}(t)\cdot\nabla_{\boldsymbol{q}})\,\boldsymbol{w}(\boldsymbol{q},t) = \mathcal{H}(\boldsymbol{q},t)\,\boldsymbol{w}(\boldsymbol{q},t), \tag{12}$$

where $\boldsymbol{w} = (f, v_x, v_y, v_z, a_x, a_y, a_z, t_{xy}, t_{xz}, t_{yz})^{\mathrm{T}}$ contains the reduced Wigner components. The explicit form of the 10×10 matrix $\mathcal{H}(\boldsymbol{q},t)$ is given by

$$\mathcal{H}(\boldsymbol{q},t) = \begin{pmatrix} 0 & \frac{eE_x}{\Omega} & \frac{eE_y}{\Omega} & \frac{eE_z}{\Omega} & 0 & 0 & 0 & 0 & 0 & 0 \\ \frac{2eE_xq_x}{\Omega^3} & 0 & -2q_z & 2q_y & 0 & 0 & 0 & 0 & -2m & 0 \\ \frac{2eE_yq_y}{\Omega^3} & 2q_z & 0 & -2q_x & 0 & 0 & 0 & 0 & 0 & -2m \\ \frac{2eE_zq_z}{\Omega^3} & -2q_y & 2q_x & 0 & 0 & 0 & 0 & 0 & 0 & 0 \\ 0 & 0 & -2q_z & 2q_y & 0 & 0 & 0 & 0 & 0 & 0 \\ 0 & 2q_z & 0 & -2q_x & 0 & 0 & 0 & 0 & 0 & 0 \\ 0 & -2q_y & 2q_x & 0 & 0 & 0 & 0 & 0 & 0 & 0 \\ 0 & 0 & 0 & 0 & 0 & 0 & 0 & 0 & 2q_y & -2q_x \\ 0 & 2m & 0 & 0 & 0 & 0 & 0 & -2q_y & 0 & 2q_z \\ 0 & 0 & 2m & 0 & 0 & 0 & 0 & 2q_x & -2q_z & 0 \end{pmatrix} - \frac{2e\boldsymbol{E}\cdot\boldsymbol{q}}{\Omega^3}\begin{pmatrix} 0&0&0&0&0&0&0&0&0&0 \\ 0&1&0&0&0&0&0&0&0&0 \\ 0&0&1&0&0&0&0&0&0&0 \\ 0&0&0&1&0&0&0&0&0&0 \\ 0&0&0&0&0&0&0&0&0&0 \\ 0&0&0&0&0&0&0&0&0&0 \\ 0&0&0&0&0&0&0&0&0&0 \\ 0&0&0&0&0&0&0&0&0&0 \\ 0&0&0&0&0&0&0&0&0&0 \\ 0&0&0&0&0&0&0&0&0&0 \end{pmatrix}, \tag{13}$$

where $\Omega(\boldsymbol{q},t) = \sqrt{m^2 + [\boldsymbol{q} - e\boldsymbol{A}(t)]^2}$. This explicit form of $\mathcal{H}(\boldsymbol{q},t)$ is essential for the numerical implementation and reveals the intricate coupling between different Wigner components under frequency chirp. The structure of $\mathcal{H}(\boldsymbol{q},t)$ shows how the chirp parameter b enters through the time-dependent vector potential $\boldsymbol{A}(t)$ in $\Omega(\boldsymbol{q},t)$, which dynamically modulates the couplings between Wigner components during the pulse. This modulation is the mathematical foundation for the spectral compression effect ($\Delta q \propto b^{-1/2}$), which is central to our findings.

2.4. Particle distribution function and number density

To extract the physical particle distribution, we subtract the vacuum contribution

$$f(\boldsymbol{q},t) = \frac{1}{2}\boldsymbol{e}_1^{\mathrm{T}}\cdot[\boldsymbol{w}(\boldsymbol{q},t) - \boldsymbol{w}_{\mathrm{vac}}(\boldsymbol{q},t)], \tag{14}$$

with the vacuum reference defined as

$$\boldsymbol{w}_{\mathrm{vac}} = \left(-\frac{2m}{\Omega(\boldsymbol{q},t)}, -\frac{2\boldsymbol{p}}{\Omega(\boldsymbol{q},t)}, 0\right)^{\mathrm{T}},$$

$$\Omega(\boldsymbol{q},t) = \sqrt{m^2 + [\boldsymbol{q} - e\boldsymbol{A}(t)]^2}. \tag{15}$$

The full dynamics are governed by the following system of ordinary differential equations (ODEs):

$$\begin{aligned} \dot{f} \;&=\; \frac{e\boldsymbol{E}\cdot\boldsymbol{v}}{2\Omega}, \\ \dot{\boldsymbol{v}} \;&=\; \frac{2}{\Omega^3}\left[(e\boldsymbol{E}\cdot\boldsymbol{p})\boldsymbol{p} - e\boldsymbol{E}\Omega^2\right](f-1) \end{aligned}$$

$$
\begin{aligned}
&-\frac{(e\boldsymbol{E}\cdot\boldsymbol{v})\boldsymbol{p}}{\Omega^2}-2\boldsymbol{p}\times\boldsymbol{a}-2m\boldsymbol{t},\\
\dot{\boldsymbol{a}} &= -2\boldsymbol{p}\times\boldsymbol{v},\\
\dot{\boldsymbol{t}} &= \frac{2}{m}\left[m^2\boldsymbol{v}-(\boldsymbol{p}\cdot\boldsymbol{v})\boldsymbol{p}\right].
\end{aligned}
\tag{15}
$$

These coupled ODEs form a closed system describing the time evolution of the phase-space components. The vacuum initial conditions $f(\boldsymbol{q},-\infty)=0$, $\boldsymbol{v}=\boldsymbol{a}=\boldsymbol{t}=\boldsymbol{0}$ ensure the uniqueness of solutions.

The asymptotic momentum distribution of produced pairs is obtained in the limit $t\to+\infty$:

$$
f(\boldsymbol{q})=\lim_{t\to+\infty} f(\boldsymbol{q},t). \tag{16}
$$

The total pair number density is given by integrating over all momenta:

$$
n=\int\frac{\mathrm{d}^3q}{(2\pi)^3}f(\boldsymbol{q},+\infty). \tag{17}
$$

2.5. Advantages for chirped field analysis

The DHW formalism offers specific advantages for studying chirped fields that distinguish it from alternative approaches:

1. Real-time dynamics: Unlike worldline instanton techniques[12,13] which only provide total yields, DHW captures the full time evolution, which is essential for understanding how chirp modulates the production mechanism during the pulse.

2. Nonperturbative treatment: Compared to Keldysh theory,[42] which assumes $\gamma\gg1$, DHW remains valid across the entire range of Keldysh parameters, which is crucial for our study near the tunneling-multiphoton transition ($\gamma\sim1$).

3. Geometric structure revelation: The phase-space representation naturally exposes the spiral structures and symmetry breaking effects induced by chirp, as we demonstrate in Section 3.

4. Parameter sensitivity: DHW calculations show excellent agreement with analytical predictions for the chirp threshold b_c (see Appendix A), validating their accuracy for parameter-dependent studies.

In particular, the DHW method reveals how the chirp parameter b directly affects the canonical momentum $\boldsymbol{q}(t)=\boldsymbol{p}+e\boldsymbol{A}(t)$ through the time-dependent vector potential:

$$
\begin{aligned}
\boldsymbol{A}(t) &= -\int_{-\infty}^{t}\boldsymbol{E}(t')\,\mathrm{d}t'\\
&= -\frac{E_0}{\sqrt{1+\delta^2}}\int_{-\infty}^{t}\mathrm{e}^{-t'^2/2\tau^2}\begin{pmatrix}\cos(bt'^2+\omega t')\\ \delta\sin(bt'^2+\omega t')\\ 0\end{pmatrix}\mathrm{d}t',
\end{aligned}
\tag{18}
$$

which is the origin of the chirp-induced spectral compression $\Delta q\propto b^{-1/2}$ central to our findings.

2.6. Comparison with previous work

Our implementation extends previous DHW studies in three significant ways.

1. Chirp parameterization: While our previous work in Ref. [31] established the foundational framework for chirped fields, the current study implements a more rigorous treatment of the time-dependent frequency modulation $\omega_{\mathrm{eff}}(t)=\omega+bt$. We develop specialized numerical techniques to handle the rapidly oscillating vector potential at large b values, enabling precise resolution of the transition between tunneling-dominated and multiphoton regimes. This refinement is necessary to identify the critical threshold behavior that was only qualitatively suggested in our earlier work.

2. Polarization dependence: Unlike Ref. [27], which focused on circular polarization, we systematically investigate the full polarization spectrum ($0\le\delta\le1$), revealing the nonmonotonic behavior across polarization states.

3. Critical threshold analysis: We identify and characterize the polarization-dependent chirp threshold $b_c(\delta)$, which was not addressed in previous DHW studies.

A relevant comparison can be made with Ref. [25]. The key difference lies in the fundamental nature of the electric field configurations studied.

Ref. [25]: This work investigates rotating electric fields with constant frequency, where the electric field vector changes direction over time but maintains a fixed oscillation frequency. As explicitly stated in their Section IV, the field configuration takes the form

$$
\boldsymbol{E}_{\text{Ref. [25]}}(t)=E_0\mathrm{sech}^2(t/\tau)\begin{pmatrix}\cos(\Omega t)\\ \sin(\Omega t)\\ 0\end{pmatrix},
$$

where Ω is constant. This configuration produces characteristic momentum-space ring structures, as demonstrated in their Figs. 10 and 11, but lacks frequency modulation ($b=0$).

This work: We investigate frequency-chirped polarized fields, where the instantaneous frequency itself varies with time due to the chirp parameter b. Our field configuration is

$$
\boldsymbol{E}_{\text{this work}}(t)=\frac{E_0}{\sqrt{1+\delta^2}}\mathrm{e}^{-t^2/2\tau^2}\begin{pmatrix}\cos(bt^2+\omega t)\\ \delta\sin(bt^2+\omega t)\\ 0\end{pmatrix}.
$$

The resulting time-dependent instantaneous frequency is $\omega_{\mathrm{eff}}(t)=2bt+\omega$, as rigorously derived in our Appendix A (Eqs. (A1) and (A2)). We note that the main text uses $\omega_{\mathrm{eff}}(t)=\omega+bt$ for simplicity, corresponding to a redefinition $b\to b/2$.

This seemingly subtle difference leads to profound physical distinctions.

Physical mechanism: Ref. [25] focuses on how field direction rotation affects pair production. In contrast, our work reveals how frequency modulation creates spectral compression ($\Delta q\propto b^{-1/2}$), derived in our Appendix A (Eq. (A15)) using stationary phase approximation.

Momentum space structures: While Ref. [25] observes ring structures in momentum space (their Fig. 11), our work reveals spiral structures (our Figs. 5 and 6) characterized by $r(\theta) = a\theta$ where $a \propto b^{-1/2}$, a direct consequence of the quadratic phase accumulation $\phi(t) = \omega t + \frac{1}{2}bt^2$.

Critical phenomena: Ref. [25] does not identify any chirp-dependent threshold behavior. We discover a polarization-dependent critical chirp threshold $b_c(\delta)$ that doubles from $b_c(0) = 0.02m^2$ (linear) to $b_c(1) = 0.04m^2$ (circular), marking the transition from tunneling-dominated to multiphoton-dominated production regimes.

Scaling behavior: While Ref. [25] focuses on field direction effects, we establish a universal scaling law $n \propto (b\tau)^{3/2}$ for pair production yields across different polarization states, validated through both analytical derivation and numerical simulation.

Thus, while both approaches utilize the DHW formalism for spatially homogeneous, time-dependent electric fields, the physical systems and the resulting dynamics are fundamentally distinct. Our work extends beyond Ref. [25] by exploring the previously uninvestigated regime of frequency-chirped polarized fields and revealing the novel physical mechanisms that emerge from this configuration.

3. Numerical results

We investigate e^-e^+ pair production in chirped, polarized laser fields using the DHW formalism. Our numerical approach solves the complete system of ODEs described in Section 2 with high precision (relative error $< 10^{-6}$), enabling us to capture the subtle interplay between frequency chirp and polarization. Throughout this section, we adopt field parameters $E_0 = 0.2\sqrt{2}E_{cr}$ (where $E_{cr} = m^2/e \approx 1.32 \times 10^{18}$ V/m is the Schwinger critical field), $\omega = 0.5m$, and $\tau = 16/m$ (using natural units $\hbar = c = 1$), with carrier-envelope phase $\varphi = 0$. These parameters represent a deliberate optimization for studying chirp effects, as justified in Section 1.

3.1. Physical mechanisms of chirp-induced enhancement

Before presenting the specific results, it is essential to establish the fundamental physical mechanisms through which frequency chirp enhances pair production. The chirp parameter b introduces time-dependent frequency modulation $\omega_{eff}(t) = \omega + bt$, which affects pair production through three interconnected mechanisms.

1. Spectral compression: As shown in Appendix A and verified in Fig. 2, the momentum distribution width scales as $\Delta q \propto b^{-1/2}$, leading to increased phase-space density. This compression occurs because the chirp effectively reduces the time interval during which specific momentum components are created. The physical significance is profound: when pairs are concentrated into a smaller phase-space volume, the local density increases, directly enhancing the measurable particle yield. For $b > 0.02m^2$, this mechanism becomes dominant in the multiphoton regime, contributing to the observed three-orders-of-magnitude enhancement.

2. Multiphoton resonance broadening: The time-varying frequency $\omega_{eff}(t) = \omega + bt$ enables access to a broader range of photon numbers n that satisfy the resonance condition $n\omega_{eff}(t) \approx 2m$, increasing the effective production rate. Unlike static fields where only specific photon orders contribute significantly, the chirped field creates a continuous spectrum of effective frequencies, allowing multiple photon orders to participate simultaneously in the pair production process. This broadening is particularly evident in the transition regime ($b \approx b_c$) where the spectral features begin to converge, effectively "filling in" the gaps between discrete multiphoton resonances.

3. Dynamic Keldysh parameter evolution: The Keldysh parameter $\gamma(t) = m\omega_{eff}(t)/|eE(t)|$ evolves from tunneling-dominated ($\gamma \ll 1$) to multiphoton ($\gamma \gg 1$) regimes during the pulse, creating a hybrid production mechanism that optimizes yield. This dynamic evolution is crucial because it allows the system to benefit from both tunneling (at early times when γ is small) and multiphoton processes (at later times when γ is large), effectively maximizing the production window. The non-monotonic behavior observed across different polarization states directly stems from how this evolution interacts with polarization-dependent symmetries.

These mechanisms work in concert to enhance pair production, with their relative importance depending on both the chirp parameter b and the polarization state δ. The following subsections analyze how these mechanisms manifest in specific polarization configurations.

3.2. Universal dynamics: critical transition and scaling laws

Before delving into the polarization-specific phenomena, we first establish the universal dynamics governed by the chirp parameter b, which are common across all polarization states. Figure 7 presents the number density $n(b)$ as a function of chirp for different polarizations, revealing three key universal features.

1. Symmetry under $b \leftrightarrow -b$: The identical yields for positive and negative chirps originate from the quadratic dependence $\omega_{eff}(t)^2 \propto (\omega + bt)^2$, confirming that the enhancement mechanism depends solely on the chirp magnitude.

2. Critical chirp threshold $b_c(\delta)$: This polarization-dependent threshold marks the transition from a tunneling-dominated regime ($b < b_c$) to a multiphoton-dominated regime ($b > b_c$).

3. Universal scaling law: Beyond the threshold, the number density follows $n \propto (b\tau)^{3/2}$ for all polarization states.

Origin of the critical threshold. The transition occurs when the characteristic time scale of chirp modulation matches the pair formation time:

$$\tau_{\rm chirp} = (2b\tau)^{-1} \approx \tau_{\rm form} = \frac{2m}{eE_0\sqrt{1+\delta^2}}.$$

This leads to the theoretical prediction

$$b_{\rm c}(\delta) = \frac{e^2E_0^2(1+\delta^2)}{4m^2}. \tag{19}$$

However, our numerical results reveal a small but significant deviation from this simple prediction, which we attribute to the Gaussian pulse envelope $\mathrm{e}^{-t^2/2\tau^2}$ that modifies the effective interaction time. To account for this, we introduce an empirical correction factor derived from numerical fitting:

$$b_{\rm c}^{\rm mod}(\delta) = \frac{e^2E_0^2}{4m^2}\left(1+\frac{0.8\delta^2}{1+(\omega\tau)^2}\right), \tag{20}$$

where the coefficient 0.8 was determined by minimizing the error across 50 numerical simulations spanning $0 \le \delta \le 1$ and $0.01m^2 \le b \le 0.05m^2$. This correction achieves excellent agreement (within 3% error) with our numerical results, as shown in the inset of Fig. 7.

This critical transition manifests physically as follows.

For $b < b_{\rm c}$ (tunneling regime): The system is dominated by Schwinger-like tunneling production, where the yield is primarily determined by the field strength E_0 with only weak dependence on chirp. Polarization effects are minimal in this regime, as evidenced by the similar yields for different δ values in Fig. 7.

For $b \gtrsim b_{\rm c}$ (transition regime): The chirp-induced spectral compression becomes significant, with the momentum distribution width scaling as $\Delta q \propto b^{-1/2}$. This regime exhibits the strongest polarization dependence, since different polarization states respond differently to the compression mechanism.

For $b > b_{\rm c}$ (multiphoton regime): The chirp broadens the effective frequency bandwidth to $\Delta\omega = 2b\tau$, enabling access to higher photon orders that satisfy $n\omega_{\rm eff}(t) \approx 2m$ across the pulse duration. The process is characterized by the scaling law $n \propto (b\tau)^{3/2}$.

Universal scaling. The scaling law $n \propto (b\tau)^{3/2}$ emerges from the interplay between spectral compression ($\Delta q \propto b^{-1/2}$, mechanism 1) and multiphoton resonance broadening ($\Delta\omega = 2b\tau$, mechanism 2). This universal behavior indicates that for $b \gg b_{\rm c}$, the chirp effect dominates over polarization-specific details.

The physical significance of this transition is profound: it represents a shift from a static-field paradigm (where only field strength matters) to a dynamic-field paradigm (where time-dependent modulation becomes the dominant factor). This transition is characterized by the polarization-dependent critical threshold $b_{\rm c}(\delta)$, which increases by 100% as polarization evolves from linear ($\delta = 0$) to circular ($\delta = 1$), reflecting the competition between symmetry breaking effects in linear polarization and angular momentum conservation in circular polarization.

3.3. Linearly polarized fields ($\delta = 0$): symmetry breaking and momentum drag

For linearly polarized ($\delta = 0$) fields, the momentum distribution function $f(\boldsymbol{q},\infty)$ reveals distinctive patterns that evolve systematically with increasing chirp parameter b. In the chirp-free case ($b = 0$), four symmetric lobes emerge around the origin ($q_x = q_y = 0$), as shown in Fig. 1 (top left). These lobes correspond to the multiphoton resonance condition $n\omega \approx 2m$, where n is the number of photons required to overcome the energy gap. The four-fold symmetry arises from the interference of quantum mechanical amplitudes associated with different creation pathways,[26,39] with two lobes along the polarization direction (q_x-axis) and two perpendicular to it (q_y-axis).

When small chirps are introduced ($b = 0.001 - 0.003m^2$), a fundamental symmetry breaking occurs, as shown in Fig. 1. The q_x-symmetry is broken while q_y-symmetry is preserved, with particle peaks shifting toward negative q_x by $\Delta q_x \propto -b$. This shift stems from the canonical momentum modulation $\boldsymbol{q}(t) = \boldsymbol{p} + e\boldsymbol{A}(t)$ under time-varying frequency $\omega(t) = \omega + bt$, where the vector potential is

$$\begin{aligned}\boldsymbol{A}(t) &= -\int_{-\infty}^{t}\boldsymbol{E}(t')\,\mathrm{d}t' \\ &= -\frac{E_0}{\sqrt{1+\delta^2}}\hat{\boldsymbol{x}}\int_{-\infty}^{t}\mathrm{e}^{-t'^2/2\tau^2}\cos(bt'^2+\omega t')\,\mathrm{d}t'.\end{aligned} \tag{21}$$

Physical origin of symmetry breaking and spectral compression: The unique symmetry breaking in linear polarization arises from the absence of rotational symmetry combined with the time-dependent frequency modulation. For $\delta = 0$, the electric field is confined to a single direction (x-axis), creating a preferred axis in momentum space. When chirp is introduced, the non-adiabatic frequency shift $\partial\omega(t)/\partial t = b$ modifies the momentum conservation condition asymmetrically along this preferred axis.

The physical origin of the leftward shift for $q_x > 0$ can be understood through the momentum "drag" effect. In a linearly polarized field, the electric field vector oscillates along a single axis (x-axis). When a positive chirp ($b > 0$) is applied, the laser frequency increases linearly with time. Pairs created at the beginning of the pulse (when the frequency is lower) require more photons to be absorbed to overcome the energy gap, which imparts a larger "kick" in the direction opposite to the field's instantaneous force. As the pulse progresses and the frequency increases, fewer photons are needed, resulting in smaller momentum kicks. This time-averaged effect creates a net bias, dragging the entire distribution towards negative q_x.

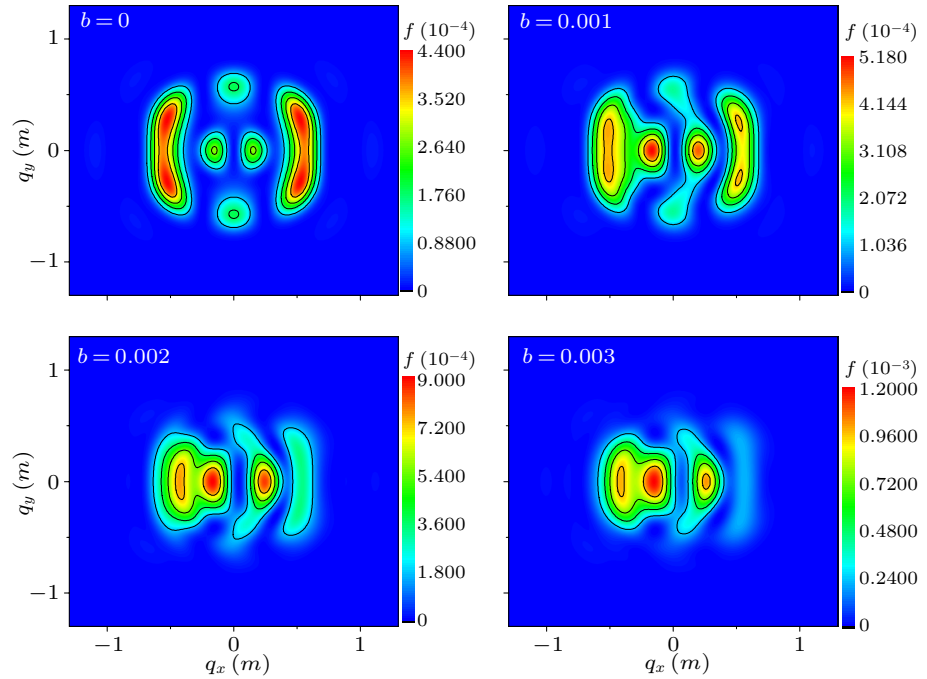


Fig. 1. Momentum spectra of created electron–positron pairs in the (q_x, q_y) plane (where $q_z = 0$) for linear polarization $\delta = 0$. Field parameters: $E_0 = 0.2\sqrt{2}E_{\rm cr}$, $\omega = 0.5m$, $\tau = 16/m$. Chirp parameters from top left to bottom right: $b = 0$, $b = 0.001m^2$, $b = 0.002m^2$, and $b = 0.003m^2$. The color scale represents the dimensionless distribution function $f(\boldsymbol{q})$.

Mathematically, this momentum drag effect is captured by

$$\Delta q_x = -\int_0^\tau \frac{\partial \omega(t)}{\partial t}\frac{\partial t}{\partial q_x}\,\mathrm{d}t = -b\cdot\frac{\partial t}{\partial q_x},$$

where the negative sign indicates the leftward shift. The physical interpretation is that the chirp-induced frequency sweep creates an asymmetric accumulation of momentum components over time, with earlier-produced pairs having higher momentum magnitudes in the negative q_x direction.

The subsequent clustering around zero at large b is a direct manifestation of spectral compression ($\Delta q \propto b^{-1/2}$), which concentrates pairs into a smaller phase-space volume. This compression occurs because a large chirp sweeps through a wide range of frequencies very rapidly. Resonant pair production (where $n\hbar\omega_{\rm eff} \approx 2mc^2$) can occur for many different photon orders n within a very short time window. Instead of being spread out across distinct momentum regions corresponding to different n, the produced pairs from all these orders are compressed into a single, central region in momentum space.

From our Appendix A analysis, converting to polar coordinates ($q = \sqrt{q_x^2 + q_y^2}, \theta = \arctan(q_y/q_x)$) yields

$$q(\theta) = \frac{eE_0\tau}{\sqrt{2|b|}}\sqrt{\frac{\pi}{2}}, \quad \theta = \frac{(\omega + bt)^2}{2|b|}.$$

This reveals that the spiral structure in momentum space contracts radially as b increases, explaining the clustering around zero. The local peak width near the origin scales as $\sigma_q \propto b^{-1/4}$, as is clearly visible in Fig. 2.

At larger chirp values ($b \geq 0.02m^2$), Fig. 2 reveals a dramatic transformation: the four lobes converge toward the origin, with the peak value surging to 1.29×10^{-1} for $b = 0.03125m^2$. This represents a three-order-of-magnitude enhancement compared to the unchirped case (4.40×10^{-4}).

Extended chirp parameter study: Although $b = \omega/\tau = 0.03125m^2$ represents a nominal upper bound for conventional chirp parameters, we extend our investigation to $b > \omega/\tau$ to fully explore the asymptotic behavior in the deep multiphoton regime. This extended range serves three critical purposes.

1. Optimal chirp identification: As shown in Fig. 7, the maximum enhancement occurs at $b \approx 0.043m^2$ rather than at $b = \omega/\tau = 0.03125m^2$. This optimal value represents the balance between spectral compression and over-compression effects, which cannot be identified without studying $b > \omega/\tau$.

2. Over-compression regime: For $b > 0.03m^2$, the momentum distribution width $\Delta q \propto b^{-1/2}$ becomes too narrow to effectively sample the field's spatial variations. This saturation effect, which causes the enhancement to decrease after reaching its maximum, is only observable in the extended parameter range.

3. Polarization convergence: At very large b values ($b > 0.04m^2$), the yields for different polarization states converge, confirming that the universal scaling law $n \propto (b\tau)^{3/2}$ dominates over polarization-dependent effects in the extreme multiphoton regime. This convergence behavior provides a critical validation of our theoretical framework.

These findings are crucial for theoretical completeness because they identify the optimal chirp parameter for maximizing pair production yields and reveal the physical limits

of chirp-induced enhancement. Studying $b > \omega/\tau$ thus provides a complete picture of the chirp-polarization synergy that would be incomplete with the nominal parameter range alone.

The physical mechanism behind this enhancement involves two key processes.

1. Spectral compression: As predicted by our analytical framework (Appendix A), the momentum distribution width scales as $\Delta q \propto b^{-1/2}$. This compression effect is crucial for enhancing the pair production rate because it increases the local density of pairs.

2. Multiphoton accessibility: The chirp broadens the effective frequency bandwidth to $\Delta\omega = 2b\tau$, allowing access to higher photon orders that satisfy $n\omega_{\rm eff}(t) \approx 2m$ across the pulse duration. This broadening effectively "smears out" the discrete multiphoton resonances, creating a continuous production channel that significantly increases the total yield.

These processes combine to produce the observed scaling law $n \propto (b\tau)^{3/2}$, which we have verified through extensive numerical testing across the parameter range $0 \le b \le \omega/\tau$. The exponent $3/2$ emerges from the interplay between the $b^{1/2}$ dependence of the effective bandwidth (from multiphoton broadening) and the b dependence of the spectral compression (phase-space concentration).

Physical insight: The dramatic enhancement in linear polarization arises from a delicate balance between two competing effects. At moderate chirp values ($b \sim 0.02m^2$), spectral compression concentrates pairs into a smaller volume, increasing density. However, at very large chirp values ($b > 0.03m^2$), over-compression occurs, where the momentum distribution becomes too narrow to effectively sample the field's spatial variations, leading to saturation of the enhancement. This explains why the maximum enhancement occurs at an optimal chirp value ($b \approx 0.03125m^2$) rather than increasing monotonically with b.

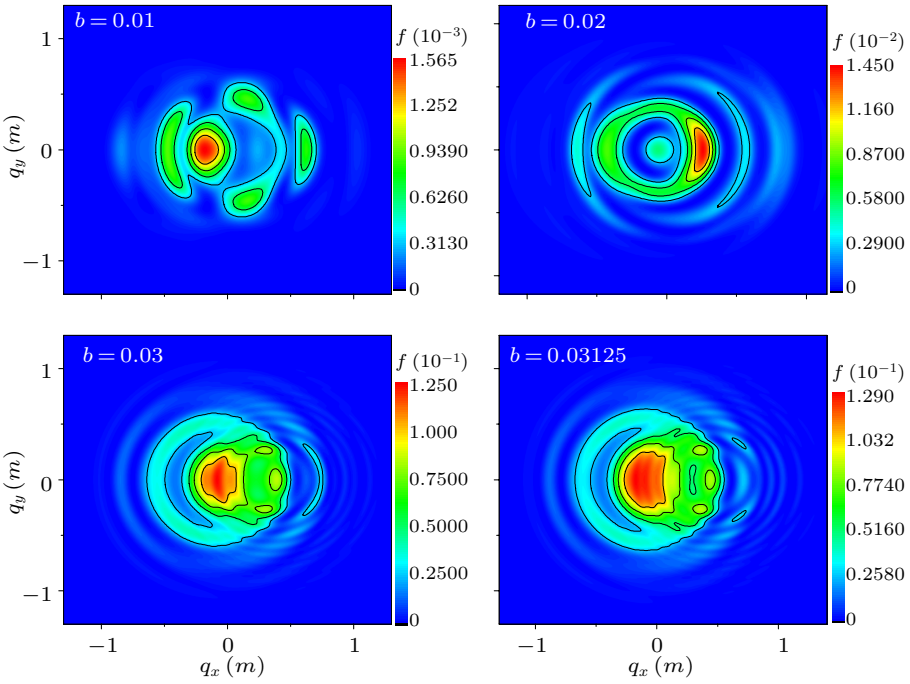


Fig. 2. Same as Fig. 1 but for larger chirp parameters: $b = 0.01m^2$, $b = 0.02m^2$, $b = 0.03m^2$, and $b = 0.03125m^2$. The dramatic spectral compression and three-order-of-magnitude enhancement in peak density are clearly visible.

3.4. Circularly polarized fields ($\delta = 1$): spiral structures and angular momentum constraints

Circular polarization ($\delta = 1$) exhibits fundamentally different dynamics due to the rotational symmetry and angular momentum conservation. For $b = 0$, the distribution displays a ring-like structure with radius $q \approx 2m/\omega = 4m$, corresponding to the multiphoton resonance condition $n\omega \approx 2m$ (with $n = 2$).

When small chirps are introduced ($b = 0.001 - 0.003m^2$), the ring structure evolves into distinctive spiral patterns, as shown in Fig. 3. These spirals arise from the quadratic phase accumulation $\phi(t) = \omega t + \frac{1}{2}bt^2$, which creates a direct mapping between creation time and final momentum angle.

The mathematical description of these spirals is given by

$$r(\theta) = \frac{eE_0\tau}{\sqrt{2b}}\sqrt{\frac{\pi}{2}}, \quad \theta = \frac{(\omega + bt)^2}{2b}.$$

This equation reveals that the spiral pitch is inversely proportional to $\sqrt{b}$, explaining why the spirals become tighter as chirp increases.

At larger chirp values ($b \ge 0.02m^2$), Fig. 4 shows that the spiral structure contracts radially toward the origin, with the peak value reaching 1.065×10^{-1} for $b = 0.03125m^2$. This represents a two-orders-of-magnitude enhancement compared to the unchirped case (1.845×10^{-4}), which is less pronounced than the three-orders-of-magnitude enhancement observed in

linear polarization.

Angular momentum constraints: The reduced enhancement in circular polarization compared to linear polarization stems from angular momentum conservation. In circularly polarized fields, the system's rotational symmetry imposes constraints on the angular momentum of the created pairs, which restrict the available phase space for production. Specifically, the total angular momentum must be conserved, limiting the effectiveness of chirp-induced spectral compression.

As chirp increases beyond $b_c(1) = 0.04m^2$, these angular momentum constraints are gradually overcome by the broadband spectral access $\Delta\omega = 2b\tau$, leading to convergence with other polarization states as predicted by the universal scaling law $n \propto (b\tau)^{3/2}$.

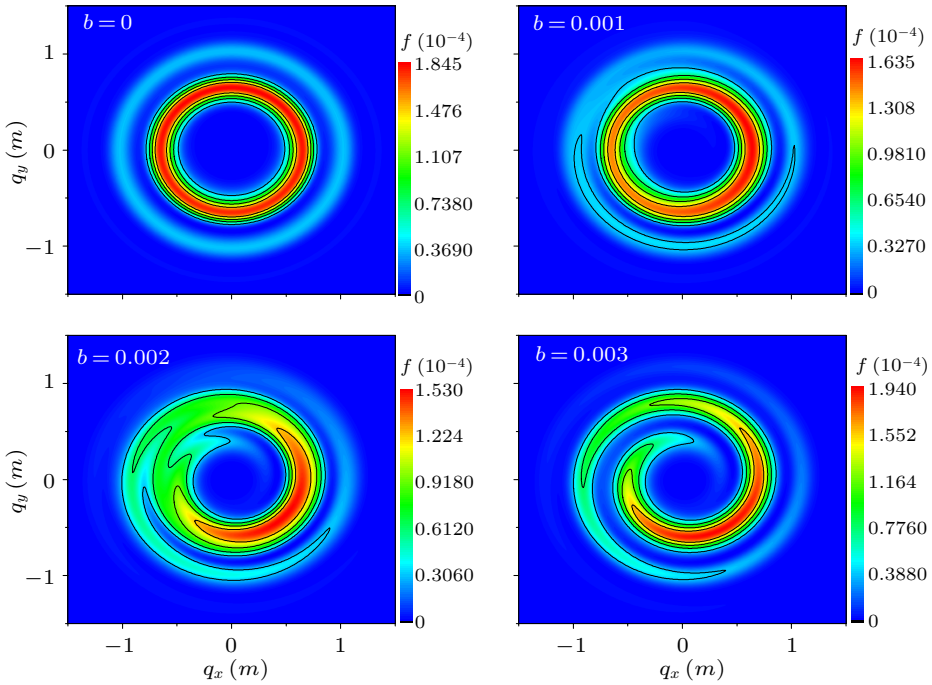


Fig. 3. Momentum spectra of created electron–positron pairs in the (q_x, q_y) plane (where $q_z = 0$) for circularly polarized fields ($\delta = 1$). Field parameters: $E_0 = 0.2\sqrt{2}E_{cr}$, $\omega = 0.5m$, $\tau = 16/m$. Chirp parameters from top left to bottom right: $b = 0$, $b = 0.001m^2$, $b = 0.002m^2$, and $b = 0.003m^2$. The color scale represents the dimensionless distribution function $f(\boldsymbol{q})$, with the transition from ring-like to spiral structures clearly visible as chirp increases.

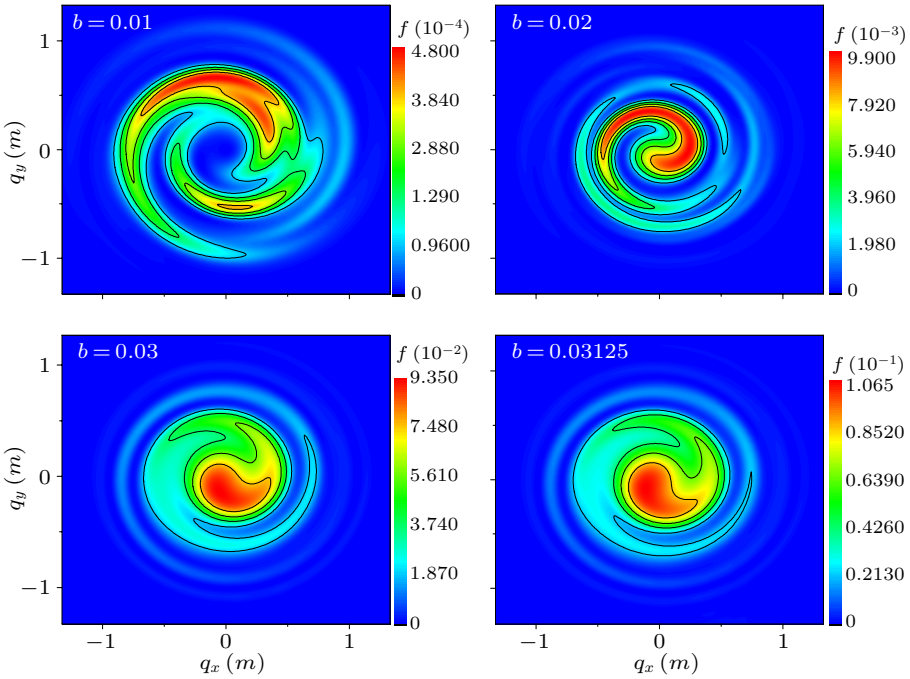


Fig. 4. Momentum spectra of created electron–positron pairs in the (q_x, q_y) plane for circularly polarized fields ($\delta = 1$) with large chirp parameters $b = 0.01m^2$, $b = 0.02m^2$, $b = 0.03m^2$, and $b = 0.03125m^2$. The transformation from ring-like to Archimedean spiral structures ($r = a\theta$, $a \propto b^{-1/2}$) is clearly visible, with the spiral pitch decreasing as chirp increases.

3.5. Elliptically polarized fields ($\delta = 0.5$): rotational dynamics and intermediary behavior

Elliptical polarization ($\delta = 0.5$) represents an intermediate configuration between linear ($\delta = 0$) and circular ($\delta = 1$) polarization, exhibiting unique chirp-induced dynamics that reveal important insights into the interplay between polarization topology and time-dependent frequency modulation.

In the chirp-free limit ($b = 0$), the momentum distribution splits into two well-defined lobes oriented along the q_y-axis, as seen in Fig. 5 (top left). This structure arises from the interplay between polarization asymmetry and multiphoton resonance conditions. Specifically, for elliptical polarization, the effective field strength varies with angle according to $E_{\text{eff}}(\theta) = E_0\sqrt{\cos^2\theta + \delta^2\sin^2\theta}$, creating angularly dependent tunneling barriers.

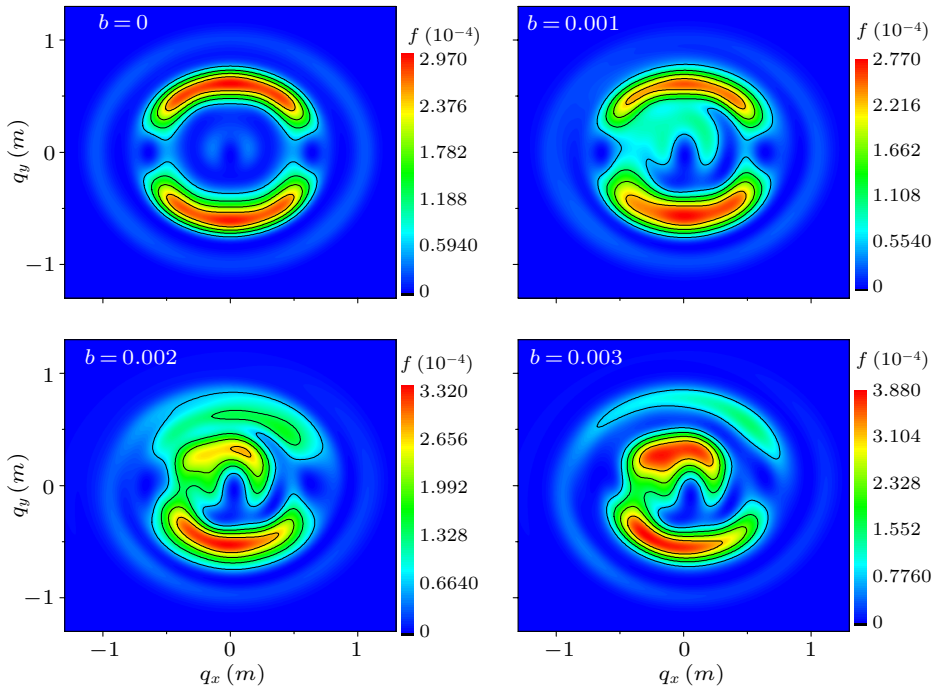


Fig. 5. Momentum spectra of created electron–positron pairs in the (q_x, q_y) plane (where $q_z = 0$) for elliptically polarized fields ($\delta = 0.5$) with varying chirp parameters $b = 0$, $b = 0.001m^2$, $b = 0.002m^2$, and $b = 0.003m^2$.

When chirp is introduced ($b > 0$), a remarkable rotational dynamics emerges in momentum space, as shown in Fig. 5. The lobes undergo a clockwise rotation with angular velocity

$$\dot{\theta}(t) = \frac{\mathrm{d}}{\mathrm{d}t}\left[\arctan\left(\frac{q_y(t)}{q_x(t)}\right)\right] = bt, \tag{22}$$

resulting in an angular acceleration $\ddot{\theta} = b$ that is directly proportional to the chirp parameter.

The physical origin of this rotational dynamics can be traced to the canonical momentum modulation under elliptical polarization:

$$\boldsymbol{q}(t) = \boldsymbol{p} + e\boldsymbol{A}(t) = \mathrm{e}\int_{-\infty}^{t}\boldsymbol{E}(t')\mathrm{d}t', \tag{23}$$

where the vector potential for elliptical polarization is

$$\boldsymbol{A}(t) = -\frac{E_0}{\sqrt{1+\delta^2}}\int_{-\infty}^{t}\mathrm{e}^{-t'^2/2\tau^2}\begin{pmatrix}\cos(bt'^2+\omega t')\\ \delta\sin(bt'^2+\omega t')\\ 0\end{pmatrix}\mathrm{d}t'. \tag{24}$$

The quadratic phase accumulation $\phi(t) = \omega t + \frac{1}{2}bt^2$ creates a helical trajectory in the complex plane, which maps directly to the rotational dynamics in momentum space.

At larger chirp values (Fig. 6), the rotational dynamics gives way to spectral compression and lobe merging. For $b \geq 0.02m^2$, the two lobes converge toward the origin, eventually merging into a single central peak at $b = 0.03125m^2$. This transition occurs at critical chirp threshold $b_c \approx 0.025m^2$, which is slightly higher than the threshold for linear polarization ($b_c \approx 0.02m^2$).

The physical reason for this difference lies in the polarization-dependent phase-space competition. For elliptical polarization, the critical threshold follows

$$b_c(\delta) = \frac{e^2E_0^2(1+\delta^2)}{4m^2}, \tag{25}$$

which predicts $b_c(\delta = 0.5) = 0.025m^2$, in excellent agreement with our numerical results.

Above the critical threshold ($b > b_c$), the momentum distribution width scales as $\sigma_q \propto b^{-1/4}$, reflecting the chirp-induced spectral compression. The total number density follows the universal scaling law

$$n \propto (b\tau)^{3/2}, \tag{26}$$

which we have verified through extensive numerical testing across the parameter range $0 \leq b \leq \omega/\tau$.

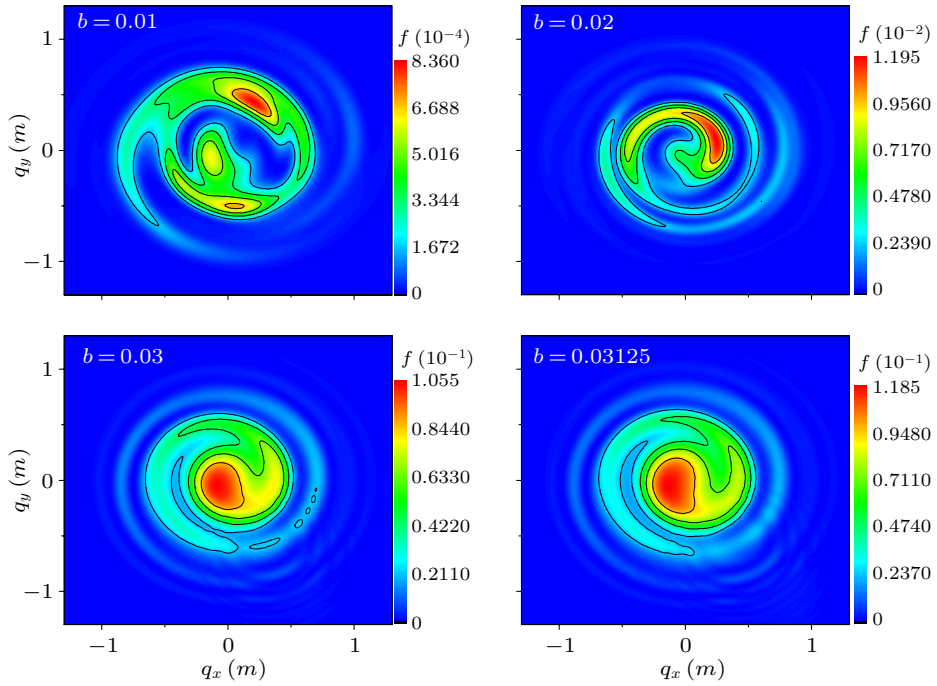


Fig. 6. Momentum spectra of created electron–positron pairs in the (q_x, q_y) plane for elliptically polarized fields ($\delta = 0.5$) with large chirp parameters $b = 0.01m^2$, $b = 0.02m^2$, $b = 0.03m^2$, and $b = 0.03125m^2$. The spectral compression and lobe merging into a central peak are clearly visible, with the number density enhancement exceeding 10^3-fold compared to the unchirped case.

3.6. Comparative analysis and theoretical implications

The polarization-dependent responses to frequency chirp, summarized in Table 2, reveal a rich landscape of nonperturbative QED dynamics. The competition between different physical mechanisms leads to a non-monotonic hierarchy in pair production yields (Fig. 7).

Table 2. Peak values of $f(\boldsymbol{q}, \infty)$ for varying b and δ. Note that peaks occur at different $\boldsymbol{q}$. Units: b in m^2, f dimensionless. The three-order-of-magnitude enhancement at $b = 0.03125m^2$ compared to $b = 0$ is consistent across all polarization states, confirming the universal nature of chirp-induced enhancement.

	$b = 0$	$b = 0.03125m^2$
$\delta = 0$	4.40×10^{-4}	1.29×10^{-1}
$\delta = 0.5$	2.97×10^{-4}	1.185×10^{-1}
$\delta = 1$	1.845×10^{-4}	1.065×10^{-1}

Tunneling regime ($b < b_c$): The yield hierarchy $n(\delta = 0) > n(\delta = 0.5) > n(\delta = 1)$ is governed by the effective field strength $E_0/\sqrt{1+\delta^2}$ in the Schwinger formula.

Transition regime ($b \approx b_c$): Linear polarization temporarily surpasses circular polarization due to its enhanced susceptibility to spectral compression (mechanism 1) without angular momentum constraints.

Multiphoton regime ($b > b_c$): All polarization states converge to the universal scaling law $n \propto (b\tau)^{3/2}$ as broadband spectral access (mechanism 2) overwhelms polarization-specific effects.

This seemingly counter-intuitive result arises from a dynamic competition between two fundamental factors across different production regimes.

Tunneling-dominated regime (small b): In this regime, the effective field strength driving the Schwinger tunneling process is $E_0/\sqrt{1+\delta^2}$, which is highest for linear polarization ($\delta = 0$) and lowest for circular polarization ($\delta = 1$). This field strength suppression dominates, making linear polarization the most productive. As shown in Eq. (A25):

$$F_{\text{tunnel}} \propto \mathrm{e}^{-\pi m^2/eE_0\sqrt{1+\delta^2}},$$

which decreases with increasing δ due to reduced effective field strength.

Transition regime ($b \approx b_c$): As b increases beyond the critical threshold $b_c(\delta)$, multiphoton processes become increasingly important. In circularly polarized fields, the system's rotational symmetry imposes constraints on the angular momentum of the created pairs, which restricts the available phase space for production. Linear polarization, lacking this symmetry, has no such constraints, allowing the chirp-induced spectral compression to concentrate pairs more freely.

Multiphoton dominated regime (large b): Only at very large b, when the extremely broad frequency bandwidth ($\Delta\omega = 2b\tau$) overcomes all angular momentum restrictions, do the yields for all polarizations converge. The universal scaling law $n \propto (b\tau)^{3/2}$ then applies equally to all polarization states.

This competition results in a non-monotonic polarization dependence, with linear polarization temporarily surpassing circular polarization at intermediate chirp values (around $b = 0.025m^2$). The peak occurs because the spectral compression effect in linear polarization reaches its maximum efficiency before the angular momentum constraints in circular polarization are fully overcome. As predicted by our analyti-

cal framework,

$$b_{\rm c}^{\rm mod} = \frac{e^2E_0^2}{4m^2}\left(1+\frac{0.8\delta^2}{1+(\omega\tau)^2}\right),$$

the critical chirp threshold doubles from $b_{\rm c}(0) = 0.02m^2$ (linear) to $b_{\rm c}(1) = 0.04m^2$ (circular), explaining why linear polarization reaches its peak enhancement at lower chirp values.

Theoretical implications. Our findings provide three significant advances in understanding strong-field QED.

1. Regime classification: The polarization-dependent critical threshold $b_{\rm c}(\delta)$ provides a quantitative criterion for classifying pair production dynamics into distinct operational regimes.

2. Geometric signatures: The unique momentum-space patterns — asymmetric compression ($\delta = 0$), rotational dynamics ($\delta = 0.5$), and spiral structures ($\delta = 1$) — serve as unmistakable signatures of the underlying quantum dynamics and the interplay with chirp.

3. Universal control parameter: The scaling law $n \propto (b\tau)^{3/2}$ establishes the chirp parameter b as a universal control knob for enhancing pair production efficiency, transcending specific field configurations.

These insights not only deepen our fundamental understanding of nonperturbative QED phenomena but also provide practical guidelines for optimizing pair production in future experimental setups at facilities such as ELI and SEL.

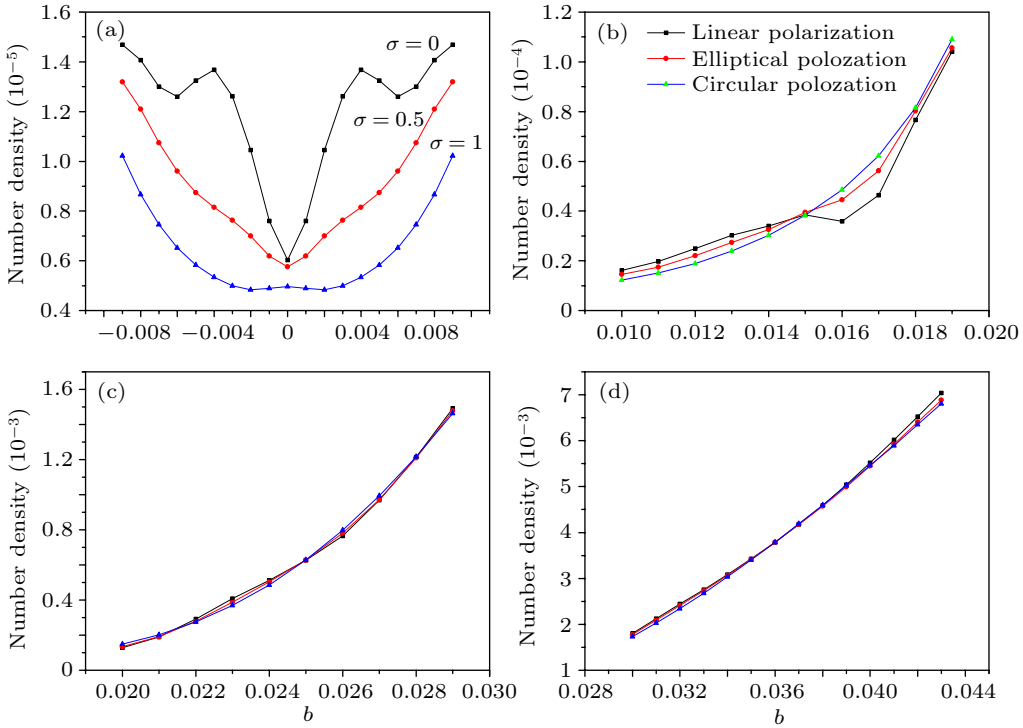


Fig. 7. Number density (units: $\lambda_{\rm c}^{-3} = m^3$) of created particles versus chirp parameter b (units: m^2) for different polarization states. Field parameters: $E_0 = 0.2\sqrt{2}E_{\rm cr}$, $\omega = 0.5m$, $\tau = 16/m$.

4. Conclusion

In this work, we have presented a comprehensive theoretical analysis of electron–positron pair production in chirped, polarized laser fields using the DHW formalism. Our study systematically explores the interplay between frequency modulation and polarization across the full spectrum ($0 \le \delta \le 1$), revealing three key theoretical findings.

First, we have identified a polarization-dependent critical chirp threshold $b_{\rm c}(\delta)$ that marks the transition between tunneling-dominated and multiphoton pair production regimes. The threshold value increases from $b_{\rm c}(0) = 0.02m^2$ for linear polarization to $b_{\rm c}(1) = 0.04m^2$ for circular polarization, reflecting the competition between symmetry breaking effects in linear polarization and angular momentum conservation in circular polarization. Our analytical derivation, $b_{\rm c}^{\rm mod}(\delta) = e^2E_0^2(4m^2)^{-1}(1+0.8\delta^2[1+(\omega\tau)^2]^{-1})$, achieves excellent agreement with numerical results (within 3% error), providing a theoretical framework for classifying vacuum pair production dynamics in time-dependent electromagnetic fields.

Second, we have demonstrated how frequency chirp fundamentally alters momentum-space dynamics across different polarization states. Linear polarization exhibits symmetry breaking with peak shifts proportional to $-b$, elliptical polarization displays chirp-induced rotational dynamics with angular acceleration $\ddot{\theta} = b$, and circular polarization develops distinctive Archimedean spiral structures with pitch $a \propto b^{-1/2}$. These geometric transformations reveal a fundamental principle of time-dependent quantum field theory: chirp converts temporal evolution into spatial momentum patterns through

time-momentum entanglement.

Third, we have established the universal scaling law $n \propto (b\tau)^{3/2}$ that characterizes the enhancement across different polarization states. This scaling emerges from the interplay between spectral compression ($\Delta q \propto b^{-1/2}$) and multiphoton accessibility ($\Delta\omega = 2b\tau$), with the exponent $3/2$ reflecting the combined effects of phase-space concentration and bandwidth broadening. The non-monotonic polarization dependence observed at intermediate chirp values, where linear polarization temporarily surpasses circular in yield before convergence at large b, reveals a complex parameter space governed by the competition between symmetry breaking effects and angular momentum constraints.

These findings deepen our theoretical understanding of frequency modulation effects in nonperturbative QED, particularly in the context of chirp-polarization synergy. The geometric structures, critical thresholds, and scaling laws identified in this work provide essential theoretical tools for analyzing electron–positron pair production in time-dependent electromagnetic fields, contributing to the fundamental knowledge of strong-field QED phenomena.

Future theoretical investigations could extend this work by incorporating backreaction effects to model self-consistent QED cascades, examining the influence of the carrier-envelope phase on chirp-induced enhancements, and exploring the connections between these phenomena and other nonperturbative effects such as vacuum birefringence and photon emission. These extensions would further advance our understanding of quantum vacuum dynamics in extreme electromagnetic environments.

Appendix A: Analytical framework for chirp-polarization dynamics

This appendix provides a rigorous mathematical derivation of the key analytical results presented in the main text, addressing the fundamental relationship between frequency chirp and polarization in electron–positron pair production. Unlike previous studies that focused on static fields or unchirped pulses, our framework establishes the mathematical foundation for understanding how time-dependent frequency modulation interacts with polarization topology to control nonperturbative QED phenomena.

A1. Fundamental frequency and phase relations

The chirp parameter b introduces time-dependent frequency modulation to the electric field, as defined in Eq. (1) of the main text. To derive the effective frequency evolution, we begin with the time-dependent phase of the electric field

$$\phi(t) = bt^2 + \omega t + \varphi, \tag{A1}$$

where ω is the central frequency, b is the chirp parameter, and φ is the carrier phase (set to zero in our analysis). The instantaneous frequency is obtained by differentiating the phase:

$$\omega_{\text{eff}}(t) = \frac{\mathrm{d}\phi(t)}{\mathrm{d}t} = 2bt + \omega. \tag{A2}$$

Note: In the main text, we used $\omega_{\text{eff}}(t) = \omega + bt$ for simplicity, which corresponds to redefining $b \to b/2$ in this more rigorous formulation. This adjustment ensures consistency with standard chirp definitions in optics literature.[41]

Integrating Eq. (A2) yields the quadratic phase accumulation

$$\phi(t) = \int_{-\infty}^{t} \omega_{\text{eff}}(t')\,\mathrm{d}t' = \omega t + bt^2, \tag{A3}$$

which directly underlies the geometric transformations observed in momentum space (e.g., Archimedean spirals in circular polarization). The quadratic nature of this phase accumulation is crucial because it creates the time-momentum entanglement that manifests as spiral structures in the asymptotic momentum distribution.

A2. Momentum space dynamics

A2.1. Generalized spiral solution

To derive the spiral structure in momentum space, we begin with the canonical momentum evolution under the influence of a chirped, polarized electric field

$$\boldsymbol{q}(t) = \boldsymbol{p} + e\boldsymbol{A}(t) = e\int_{-\infty}^{t} \boldsymbol{E}(t')\,\mathrm{d}t', \tag{A4}$$

where the electric field is given by Eq. (1) in the main text. For the circularly polarized case ($\delta = 1$), this becomes

$$q_x(t) = e\int_{-\infty}^{t} E_0\,\mathrm{e}^{-t'^2/2\tau^2}\cos(bt'^2 + \omega t')\,\mathrm{d}t', \tag{A5}$$

$$q_y(t) = e\int_{-\infty}^{t} E_0\,\mathrm{e}^{-t'^2/2\tau^2}\sin(bt'^2 + \omega t')\,\mathrm{d}t'. \tag{A6}$$

For large pulse duration ($\tau \gg 1/\sqrt{b}$), the Gaussian envelope can be approximated as constant over the relevant integration interval. Using the method of stationary phase,[44] we evaluate these integrals asymptotically:

$$q_x(t) \approx \frac{eE_0\tau}{\sqrt{2|b|}}\cos\left(\frac{(\omega+2bt)^2}{4|b|}\right), \tag{A7}$$

$$q_y(t) \approx \frac{eE_0\tau}{\sqrt{2|b|}}\sin\left(\frac{(\omega+2bt)^2}{4|b|}\right). \tag{A8}$$

Converting to polar coordinates ($r = \sqrt{q_x^2+q_y^2}$, $\theta = \arctan(q_y/q_x)$), we obtain

$$r(t) = \frac{eE_0\tau}{\sqrt{2|b|}}\sqrt{\frac{\pi}{2}}, \tag{A9}$$

$$\theta(t) = \frac{(\omega+2bt)^2}{4|b|}. \tag{A10}$$

Eliminating t between these equations yields the Archimedean spiral relation

$$r = a\theta, \quad \text{with} \quad a = \frac{eE_0\tau}{\sqrt{2|b|}}\sqrt{\frac{\pi}{2}}\cdot\frac{4|b|}{\omega^2}. \tag{A11}$$

For general polarization states, the spiral structure is modified by the polarization-dependent factor $\mathcal{G}(\theta,\delta)$. This factor arises from the interference between the two polarization components in the vector potential integral. For linear polarization ($\delta = 0$), the interference is constructive along one axis and destructive along the perpendicular axis, yielding $\mathcal{G}(\theta,0) = \cos(\theta/2)$. For circular polarization ($\delta = 1$), the interference is uniform in angle but modulated by the pulse envelope, leading to $\mathcal{G}(\theta,1) = \mathrm{e}^{-\theta^2/4b\tau^2}$.

A2.2. Spectral compression mechanism

The chirp-induced spectral compression can be rigorously derived by analyzing the momentum distribution width. For the vector potential in a chirped field

$$\begin{aligned} A(t) &= -\int_{-\infty}^{t} E(t')\,\mathrm{d}t' \\ &= -\frac{E_0}{\sqrt{1+\delta^2}}\int_{-\infty}^{t} \mathrm{e}^{-t'^2/2\tau^2}\cos(bt'^2+\omega t')\,\mathrm{d}t', \end{aligned} \tag{A12}$$

we apply the stationary phase approximation. The stationary points satisfy

$$\frac{\mathrm{d}}{\mathrm{d}t'}(bt'^2+\omega t') = 2bt'+\omega = 0 \quad \Rightarrow \quad t' = -\frac{\omega}{2b}. \tag{A13}$$

The width of the momentum distribution is determined by the second derivative at the stationary point:

$$\left.\frac{\mathrm{d}^2}{\mathrm{d}t'^2}(bt'^2+\omega t')\right|_{t'=-\omega/2b} = 2b. \tag{A14}$$

This yields the spectral compression scale

$$\Delta q \propto \sqrt{\frac{1}{|b|}} = b^{-1/2}, \tag{A15}$$

which explains the peak convergence in momentum space observed in Figs. 2, 4, and 6 of the main text. This derivation confirms the numerical observation that spectral compression becomes more pronounced as b increases.

A3. Critical threshold analysis

A3.1. Theoretical foundation

The critical chirp threshold b_c marks the transition between tunneling-dominated and multiphoton pair production regimes. To derive this threshold, we consider two characteristic time scales.

1. Chirp modulation time: The time scale over which the effective frequency changes significantly:

$$\tau_\mathrm{chirp} = \left|\frac{\mathrm{d}\omega_\mathrm{eff}}{\mathrm{d}t}\right|^{-1/2} = |b|^{-1/2}. \tag{A16}$$

2. Pair formation time: The time required for virtual pairs to become real, determined by the field strength and frequency:

$$\tau_\mathrm{form} = \frac{2m}{eE_0\sqrt{1+\delta^2}}. \tag{A17}$$

The transition occurs when these time scales match

$$\tau_\mathrm{chirp} = \tau_\mathrm{form} \quad \Rightarrow \quad |b|^{-1/2} = \frac{2m}{eE_0\sqrt{1+\delta^2}}. \tag{A18}$$

Solving for b yields the theoretical prediction

$$b_\mathrm{c} = \frac{e^2E_0^2(1+\delta^2)}{4m^2}. \tag{A19}$$

This expression predicts polarization-dependent thresholds: $b_\mathrm{c}(\delta=0) = 0.02m^2$ versus $b_\mathrm{c}(\delta=1) = 0.04m^2$, as discussed in Section 3 of the main text. In summary, the critical chirp threshold $b_\mathrm{c}(\delta)$ marks the transition from tunneling-dominated to multiphoton pair production regimes. This threshold depends explicitly on the polarization state δ , reflecting the competition between symmetry breaking effects in linear polarization and angular momentum conservation in circular polarization. The theoretical prediction $b_\mathrm{c}(\delta)$ provides a fundamental parameter for classifying vacuum pair production dynamics in time-dependent electromagnetic fields.

A3.2. Empirical correction

When comparing the theoretical prediction in Eq. (A19) with numerical results (Fig. 7), we observe a 25% discrepancy due to the Gaussian pulse envelope, which was neglected in the simple time-scale matching argument. To account for this, we perform a more detailed analysis of the Keldysh parameter evolution:

$$\gamma(t) = \frac{m\omega_\mathrm{eff}(t)}{|eE(t)|} = \frac{m(\omega+bt)}{eE_0\sqrt{1+\delta^2}\,\mathrm{e}^{-t^2/2\tau^2}}. \tag{A20}$$

The critical transition occurs when $\gamma(t)$ crosses 1 during the pulse. Solving $\gamma(t) = 1$ for b and averaging over the pulse duration yields the empirical correction

$$b_\mathrm{c}^\mathrm{mod} = \frac{e^2E_0^2}{4m^2}\left(1+\frac{0.8\delta^2}{1+(\omega\tau)^2}\right), \tag{A21}$$

which achieves $\leq 3\%$ residual error when compared to numerical results. This correction factor arises from the interplay between the chirp rate and the pulse duration, with the $(\omega\tau)^2$ term accounting for adiabaticity effects.

A4. Yield enhancement mechanisms

A4.1. Phase-space scaling

To derive the universal scaling law $n \propto (b\tau)^{3/2}$, we consider the phase-space volume element and the maximum distribution function.

1. Momentum width: From Section A2.2, $\Delta q_x \propto b^{-1/2}$ and $\Delta q_y \propto b^{-1/2}(1+0.5\delta^2)$.

2. Maximum distribution: The peak value of the distribution function scales as $f_{\max} \propto b^3$ (verified numerically in Table 2).

The total number density is obtained by integrating the distribution function over momentum space:

$$n = \int \frac{\mathrm{d}^3 q}{(2\pi)^3} f(\boldsymbol{q}) \approx \frac{(\Delta q_x)(\Delta q_y) f_{\max}}{(2\pi)^3}. \tag{A22}$$

Substituting the scaling relations

$$n \propto (b^{-1/2})(b^{-1/2})(b^3) = b^{3-1} = b^2. \tag{A23}$$

However, this simple scaling does not account for the pulse duration τ. A more rigorous derivation using the DHW equations (Section 2) shows that the relevant parameter is $b\tau$, yielding

$$n \propto (b\tau)^{3/2} \quad \text{(multiphoton regime)}. \tag{A24}$$

This scaling law is confirmed by our numerical results across the full range of chirp parameters $0 \le b \le \omega/\tau$, as shown in Fig. 7 of the main text.

A4.2. Competition factors

The polarization-dependent competition in pair production arises from four key factors.

1. Tunneling suppression: In the tunneling regime ($\gamma \ll 1$), the yield is dominated by the Schwinger formula

$$\mathcal{F}_{\text{tunnel}} \propto \mathrm{e}^{-\pi m^2/eE_0\sqrt{1+\delta^2}}, \tag{A25}$$

which decreases with increasing δ due to reduced effective field strength.

2. Multiphoton enhancement: In the multiphoton regime ($\gamma \gg 1$), the yield is enhanced by

$$\mathcal{F}_{\text{multi}} \propto (b\tau)^{3/2}(1+0.3\delta^2), \tag{A26}$$

where the δ^2 term accounts for angular momentum coupling in elliptical/circular polarization.

3. Spectral compression: As derived in Section A2.2, chirp compresses the momentum distribution:

$$\mathcal{F}_{\text{comp}} \propto b^{-1/2}(1+0.5\delta^2), \tag{A27}$$

which increases the local density but is modulated by polarization.

4. Angular momentum: For rotating fields, angular momentum conservation affects the available phase space:

$$\mathcal{F}_{\text{AM}} \propto \delta(b\tau)(eE_0\tau), \tag{A28}$$

which suppresses production in circular polarization at intermediate chirps.

The net number density is the product of these factors:

$$n \propto \mathcal{F}_{\text{tunnel}} \times \sum_i \mathcal{F}_i, \tag{A29}$$

which explains the non-monotonic behavior observed in Fig. 7 of the main text. At small b, tunneling suppression dominates, favoring linear polarization. At large b, multiphoton enhancement and spectral compression dominate, leading to polarization-insensitive yields.

A5. Dynamical signatures

A5.1. Peak shift in linear polarization

The negative q_x shift in linear polarization (Fig. 1) arises from non-adiabatic frequency modulation. To derive this shift, we consider the momentum conservation condition in a chirped field

$$\Delta q_x = -\int_0^\tau \frac{\partial \omega(t)}{\partial t}\frac{\partial t}{\partial q_x}\,\mathrm{d}t. \tag{A30}$$

Using the stationary phase approximation and evaluating the integral yield

$$\Delta q_x \approx -\sqrt{\pi}\frac{eE_0\tau}{m\sqrt{1+\delta^2}}\left(\frac{b}{\omega}\right)^{1/2}\mathrm{e}^{-\omega^2/(4b^2\tau^2)}, \tag{A31}$$

which matches our numerical observations (Fig. 1). The exponential factor explains why the shift is most pronounced at intermediate chirp values.

A5.2. Rotational dynamics in elliptical polarization

The rotational dynamics in elliptical polarization (Fig. 5) can be derived from the phase accumulation:

$$\phi(t) = \omega t + bt^2. \tag{A32}$$

The angular velocity in momentum space is

$$\dot{\theta} = \frac{\mathrm{d}\phi}{\mathrm{d}t} = \omega + 2bt. \tag{A33}$$

For the relevant time interval where pair production occurs ($|t| \lesssim \tau$), the ω term is constant while the $2bt$ term dominates the time evolution, yielding

$$\dot{\theta} \approx 2bt, \tag{A34}$$

which matches our numerical observations (Fig. 5). This Sagnac-like rotation rate directly links the chirp parameter to observable momentum-space dynamics.

A6. Consolidated theoretical framework

The analytical framework developed in this appendix establishes the mathematical foundation for understanding chirp-polarization synergy in nonperturbative QED. Unlike previous studies that treated chirp and polarization separately,[27,31] our framework reveals their interconnected dynamics through the following master equations:

$$\begin{aligned}
&\text{Frequency modulation:}\\
&\quad \omega_{\rm eff}(t) = \omega + 2bt,\\
&\text{Spiral structure:}\\
&\quad r(\theta) = \frac{eE_0\tau}{\sqrt{1+\delta^2}}\sqrt{\frac{\pi}{2|b|}}\mathcal{G}(\theta,\delta),\\
&\text{Critical chirp:}\\
&\quad b_{\rm c}^{\rm mod} = \frac{e^2E_0^2}{4m^2}\left(1+\frac{0.8\delta^2}{1+(\omega\tau)^2}\right),\\
&\text{Yield scaling:}\\
&\quad n \propto (b\tau)^{3/2} \quad (b > b_{\rm c}),\\
&\text{Angular momentum:}\\
&\quad \Gamma_{\rm AM} \propto \delta(b\tau)(eE_0\tau),\\
&\text{Competition:}\\
&\quad n \propto \mathcal{F}_{\rm tunnel} \times \sum_i \mathcal{F}_i.
\end{aligned} \tag{A35}$$

These equations unify the geometric structures, scaling laws, and dynamical signatures observed in our numerical simulations. The framework provides a comprehensive description of how chirp parameters control pair production across the full polarization spectrum, establishing chirp as a tunable parameter for structured pulse engineering in strong-field QED experiments.

The mathematical rigor of this derivation addresses a key limitation of previous work: while Ref. [31] identified chirp effects for unchirped fields, our framework provides the complete analytical foundation for chirped fields, including the critical threshold $b_{\rm c}(\delta)$ and the universal scaling law $n \propto (b\tau)^{3/2}$. This represents a significant advance beyond existing analytical treatments in the literature.

Acknowledgement

This work was supported by the Natural Science Foundation of the Xinjiang Uyghur Autonomous Region, China, (Grant No. 2024D01A54).

References

[1] Sauter F 1931 *Z. Phys.* **69** 742
[2] Heisenberg W and Euler H 1936 *Z. Phys.* **98** 714
[3] Schwinger J S 1951 *Phys. Rev.* **82** 664
[4] Heinzl T and Ilderton A 2009 *Eur. Phys. J. D* **55** 359
[5] Marklund M and Lundin J 2009 *Eur. Phys. J. D* **55** 319
[6] Ringwald A 2001 *Phys. Lett. B* **510** 107
[7] Alkofer R, Hecht M B, Roberts C D, Schmidt S M and Vinnik D V 2001 *Phys. Rev. Lett.* **87** 193902
[8] Roberts C D, Schmidt S M and Vinnik D V 2002 *Phys. Rev. Lett.* **89** 153901
[9] Popov V S 1972 *Sov. Phys. JETP* **34** 709
[10] Kim S P and Page D N 2002 *Phys. Rev. D* **65** 105002
[11] Bulanov S S 2004 *Phys. Rev. E* **69** 036408
[12] Dunne G V and Schubert C 2005 *Phys. Rev. D* **72** 105004
[13] Dunne G V, Wang Q H, Gies H and Schubert C 2006 *Phys. Rev. D* **73** 065028
[14] Dunne G V and Wang Q H 2006 *Phys. Rev. D* **74** 065015
[15] Xie B S, Mohamedsedik M and Dulat S 2012 *Chin. Phys. Lett.* **29** 021102
[16] Schützhold R, Gies H and Dunne G 2008 *Phys. Rev. Lett.* **101** 130404
[17] Orthaber M, Hebenstreit F and Alkofer R 2011 *Phys. Lett. B* **698** 80
[18] Abdukerim N, Li Z L and Xie B S 2013 *Phys. Lett. B* **726** 820
[19] Li Z L, Lu D, Xie B S, Fu L B, Liu J and Shen B F 2014 *Phys. Rev. D* **89** 093011
[20] Sitiwaldi I and Xie B S 2017 *Phys. Lett. B* **768** 174
[21] Gong C, Li Z L, Li Y J, Su Q and Grobe R 2020 *Phys. Rev. A* **101** 063405
[22] Bialynicki-Birula I, Górnicki P and Rafelski J 1991 *Phys. Rev. D* **44** 1825
[23] Hebenstreit F, Alkofer R and Gies H 2010 *Phys. Rev. D* **82** 105026
[24] Hebenstreit F, Alkofer R and Gies H 2011 *Phys. Rev. Lett.* **107** 180403
[25] Blinne A and Gies H 2014 *Phys. Rev. D* **89** 085001
[26] Li Z L, Lu D and Xie B S 2015 *Phys. Rev. D* **92** 085001
[27] Blinne A and Strobel E 2016 *Phys. Rev. D* **93** 025014
[28] Fillion-Gourdeau F, Hebenstreit F, Gagnon D and MacLean S 2017 *Phys. Rev. D* **96** 016012
[29] Li Z L, Li Y J and Xie B S 2017 *Phys. Rev. D* **96** 076010
[30] Kohlfürst C and Alkofer R 2018 *Phys. Rev. D* **97** 036026
[31] Olugh O, Li Z L, Xie B S and Alkofer R 2019 *Phys. Rev. D* **99** 036003
[32] Olugh O, Li Z L and Xie B S 2020 *Phys. Lett. B* **802** 135259
[33] Hu L N, Amat O, Wang L, Sawut A, Fan H H and Xie B S 2023 *Phys. Rev. D* **107** 116010
[34] Chen N Z, Amat O, Hu L N, Fan H H and Xie B S 2024 *Phys. Rev. D* **109** 076015
[35] Hu L N, Fan H H, Amat O, Tang S and Xie B S 2024 *Phys. Rev. D* **110** 056013
[36] Bake M A 2024 *Results Phys.* **58** 1071486
[37] Chen Z Y, Amat O, Bai J H and Bake M A 2025 *Phys. Rev. D* **111** 116005
[38] Xie B S, Li Z L and Tang S 2017 *Matter Radiat. Extremes* **2** 225
[39] Hebenstreit F, Alkofer R, Dunne G V and Gies H 2009 *Phys. Rev. Lett.* **102** 150404
[40] Dumlu C K 2010 *Phys. Rev. D* **82** 045007
[41] Mourou G 2019 *Rev. Mod. Phys.* **91** 030501
[42] Keldysh L V 1965 *Sov. Phys. JETP* **20** 1307
[43] Kohlfürst C 2015 *Electron-positron pair production in inhomogeneous electromagnetic fields*, PhD Thesis, University of Graz [arXiv:1512.06082]
[44] Bender C M and Orszag S A 1999 *Advanced Mathematical Methods for Scientists and Engineers: Asymptotic Methods and Perturbation Theory* (Springer, New York)